Communications in Applied Mathematics and Computational Science

A THIRD ORDER FINITE VOLUME WENO SCHEME FOR MAXWELL'S EQUATIONS ON TETRAHEDRAL MESHES

MARINA KOTOVSHCHIKOVA,
DMITRY K. FIRSOV AND SHIU HONG LUI

vol. 13 no. 1 2018

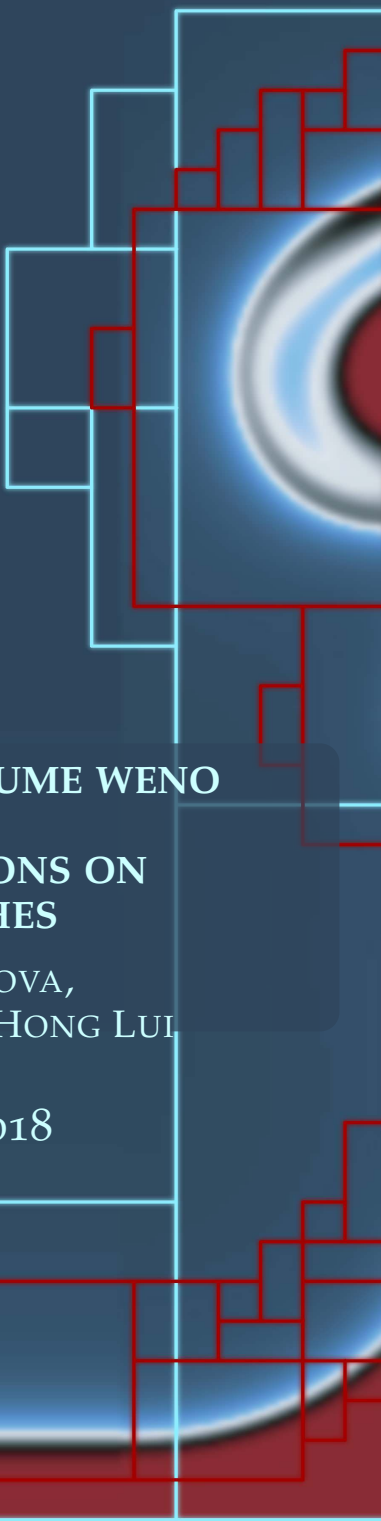

msp

COMM. APP. MATH. AND COMP. SCI.
Vol. 13, No. 1, 2018
dx.doi.org/10.2140/camcos.2018.13.87

msp

A THIRD ORDER FINITE VOLUME WENO SCHEME FOR MAXWELL'S EQUATIONS ON TETRAHEDRAL MESHES

MARINA KOTOVSHCHIKOVA, DMITRY K. FIRSOV AND SHIU HONG LUI

A third order type II WENO finite volume scheme for tetrahedral unstructured meshes is applied to the numerical solution of Maxwell's equations. Stability and accuracy of the scheme are severely affected by mesh distortions, domain geometries, and material inhomogeneities. The accuracy of the scheme is enhanced by a clever choice of a small parameter in the WENO weights. Also, hybridization with a polynomial scheme is proposed to eliminate unnecessary and costly WENO reconstructions in regions where the solution is smooth. The proposed implementation is applied to several test problems to demonstrate the accuracy and efficiency, as well as usefulness of the scheme to problems with singularities.

1. Introduction

Weighted essentially nonoscillatory (WENO) schemes are high order numerical methods developed to solve hyperbolic partial differential equations (PDEs) with solutions containing discontinuities. In a finite volume (FV) framework these schemes can be implemented on unstructured meshes making them an attractive option for solving problems with singularities due to geometry and/or inhomogeneity in material properties. For linear nondispersive media the system of Maxwell's equations is linear, and for simple geometries it can be solved analytically. In many practical applications the challenge in solving Maxwell's equations is due to complex geometrical features, broadband complex signal types, and/or inhomogeneous material properties. In these cases, finite volume time-domain (FVTD) algorithms are often implemented with success. FV schemes were adapted to Maxwell's equations from computational fluid dynamics (CFD) in the late 1980s by Shankar et al. [26] and include both central [25; 23] and upwind formulations [26; 7; 6].

The upwind FVTD formulation based on the method of characteristics and MUSCL reconstruction has shown good results on a wide range of problems. The

Kotovshchikova was supported by an NSERC postgraduate scholarship, while Lui was supported by an NSERC Discovery grant.
MSC2010: 65M08, 78M12.
Keywords: weighted essentially nonoscillatory (WENO) schemes, finite volume schemes, Maxwell's equations, tetrahedral meshes.

main drawback of the MUSCL scheme is that it is only second order accurate. Moreover, in the presence of singularities, it employs a slope limiter [5; 12] to suppress oscillations and maintain monotonicity. This unavoidably decreases the accuracy to first order at critical points. Higher order finite volume approximation schemes based on polynomial reconstruction are implemented in [22; 13]. These schemes are not a good choice for problems with nonsmooth signals or heterogeneous media nor for simulations on highly distorted meshes, where such schemes can be oscillatory or unstable. Also flux limiters when used with higher order schemes may produce results that are even less accurate than those by MUSCL schemes.

Essentially nonoscillatory (ENO) schemes were developed by Harten et al. [16] to overcome the problem of order degeneracy at critical points. Instead of using limiters to overcome a possible growth of total variation, ENO schemes use an adaptive selection of stencils according to the smoothness of the solution. Better accuracy near discontinuities is achieved by selecting the stencil that doesn't contain a singularity. ENO schemes for multidimensional unstructured meshes can be found in [15; 1; 29], and their implementations to Maxwell's equations in [9; 32].

WENO schemes were developed in [20] to improve the performance of ENO schemes. The key idea of WENO schemes is to use a weighted combination of all ENO stencils for the reconstruction. For unstructured 3D meshes there are two types of WENO schemes. Type I WENO schemes [10; 11; 31; 24] are easier to construct because the linear coefficients can be chosen as arbitrary positive numbers (usually a larger linear weight is given to the central small stencil). The accuracy of the resulting type I WENO scheme is not higher than that on each small stencil. In this work we employ the type II WENO scheme proposed by Zhang and Shu in [33] in which the weighted combination of second order reconstructions is third order accurate. The scheme is more difficult to construct for unstructured meshes as there is no freedom in selecting the linear weights. Linear weights depend solely on the mesh geometry, and in most cases there are negative weights which create stability issues. To overcome this, the criterion proposed in [21] can be used to eliminate reconstructions for which linear weights are large negative numbers.

Different modifications to the computation of nonlinear weights are suggested in the literature to improve the quality of the WENO reconstruction. For unstructured meshes the mapping technique introduced by Henrick et al. in [17] is often suggested [33; 21]. While theoretically mapping applied to third order classical WENO weights does not improve convergence, numerically this technique reduces computational errors. Another approach to improve the accuracy of WENO schemes is to modify the smoothness indicator [8]. In this work the accuracy of WENO schemes is controlled by appropriately choosing the small parameter ϵ in the WENO weights as a function of linear cell sizes. This choice was originally studied for WENO schemes on uniform meshes in 1D by Aràndiga et al. in [2].

This paper is devoted to an efficient application of the type II WENO scheme to a 3D FVTD approximation of Maxwell's equations. Based on the analysis for 1D nonuniform meshes, we implement the optimal choice of the small parameter in WENO weights for maximum achievable spatial accuracy. A threshold for very negative linear weights has been employed to eliminate possible instability. Moreover, to improve CPU time we use a criterion to determine when to apply WENO reconstruction. Basically, the WENO reconstruction is performed only for elements with large smoothness indicators in the WENO weights. The proposed implementation was tested on electromagnetic problems with analytic solutions to confirm that the accuracy and nonoscillatory effect are achieved with the proposed choices of parameters. The robustness of the type II WENO scheme for inhomogeneous media is also demonstrated numerically. Maxwell's equations are challenging due to discontinuities in the solution where the advantages of WENO schemes can be leveraged. The implementation discussed in this paper can be applied to other hyperbolic systems of PDEs.

The paper is organized as follows. Section 2 describes Maxwell's equations in time-domain and their finite volume discretization. Section 3 presents an overview of the type II finite volume WENO scheme together with improvements necessary for its efficient implementation. In Section 4, a 1D analysis of a third order WENO scheme on nonuniform meshes is discussed to support the choices made for accurate 3D applications. Finally, Section 5 presents numerical validations of the proposed implementation of a WENO scheme on tetrahedral meshes.

2. The finite volume scheme for Maxwell's equations

Consider the propagation of electromagnetic waves in a 3D heterogeneous linear isotropic medium with space varying electric permittivity $\epsilon = \epsilon(\mathbf{x})$ and magnetic permeability $\mu = \mu(\mathbf{x})$. Given a bounded region $\Omega \subset \mathbb{R}^3$, the electric field $\mathbf{E}(\mathbf{x}, \mathrm{t})$ and the magnetic field $\mathbf{H}(\mathbf{x}, \mathrm{t})$ are governed by the system of Maxwell's equations

$$\begin{cases} \epsilon \frac{\partial \mathbf{E}}{\partial \mathrm{t}} - \nabla \times \mathbf{H} = \mathbf{J}_E & \text{in } [0, T] \times \Omega, \\ \mu \frac{\partial \mathbf{H}}{\partial \mathrm{t}} + \nabla \times \mathbf{E} = \mathbf{J}_H & \text{in } [0, T] \times \Omega, \\ a\hat{\boldsymbol{n}} \times \mathbf{E} + b\hat{\boldsymbol{n}} \times (\hat{\boldsymbol{n}} \times \mathbf{H}) = 0 & \text{on } [0, T] \times \partial\Omega, \end{cases} \tag{1}$$

where $\mathbf{J}_E$ and $\mathbf{J}_H$ are the sources consisting of imposed currents and term introduced by scattered field formulation, and $\hat{\boldsymbol{n}}$ is the outward unit normal of the boundary $\partial\Omega$. Parameters a and b define different boundary conditions:

- perfect electric conductor (PEC), $a = 1$ and $b = 0$,
- perfect magnetic conductor (PMC), $a = 0$ and $b = 1$, and
- Silver–Müller absorbing boundary condition, $a = 1$ and $b = \sqrt{\mu/\epsilon}$.

Consider the normalized quantities

$$\boldsymbol{x} = l^{-1}\mathbf{x}, \qquad t = c_0 l^{-1}\mathrm{t}, \tag{2}$$

where l is a reference length, $c_0 = (\mu_0\epsilon_0)^{-1/2}$ is a dimensional speed of light in vacuum with $\epsilon_0 \approx 8.854 \cdot 10^{-12}\frac{\mathrm{A\cdot s}}{\mathrm{V\cdot m}}$, and $\mu_0 = 4\pi \cdot 10^{-7}\frac{\mathrm{V\cdot s}}{\mathrm{A\cdot m}}$. The fields $\mathbf{E}$ and $\mathbf{H}$ can be normalized to a typical electric field intensity E by

$$\boldsymbol{E} = \frac{\mathbf{E}}{E}, \qquad \boldsymbol{H} = \frac{Z_0}{E}\mathbf{H}, \qquad \boldsymbol{J}_E = \frac{lZ_0}{E}\mathbf{J}_E, \qquad \boldsymbol{J}_H = \frac{l}{E}\mathbf{J}_H, \tag{3}$$

where $Z_0 = \sqrt{\mu_0/\epsilon_0}$ is the dimensional free-space intrinsic impedance. Then the system (1) can be written in nondimensional form as

$$\begin{cases} \epsilon_r \frac{\partial \boldsymbol{E}}{\partial t} - \nabla \times \boldsymbol{H} = \boldsymbol{J}_E & \text{in } [0, c_0 l^{-1} T] \times \Omega, \\ \mu_r \frac{\partial \boldsymbol{H}}{\partial t} + \nabla \times \boldsymbol{E} = \boldsymbol{J}_H & \text{in } [0, c_0 l^{-1} T] \times \Omega, \\ a_r \hat{\boldsymbol{n}} \times \boldsymbol{E} + b_r \hat{\boldsymbol{n}} \times (\hat{\boldsymbol{n}} \times \boldsymbol{H}) = 0 & \text{on } [0, c_0 l^{-1} T] \times \partial\Omega, \end{cases} \tag{4}$$

where $\epsilon_r = \epsilon/\epsilon_0$, $\mu = \mu/\mu_0$, $a_r = a$, and $b_r = b/Z_0$. For a finite volume discretization, the first two equations of (4) are written in conservative form as

$$\boldsymbol{\alpha}\frac{\partial \boldsymbol{U}}{\partial t} + \nabla \cdot \boldsymbol{F}(\boldsymbol{U}) = \boldsymbol{J},$$

where

$$\boldsymbol{U} = \begin{bmatrix} \boldsymbol{E} \\ \boldsymbol{H} \end{bmatrix}, \qquad \boldsymbol{F}(\boldsymbol{U}) = \begin{bmatrix} \boldsymbol{F}_1(\boldsymbol{U}) & \boldsymbol{F}_2(\boldsymbol{U}) & \boldsymbol{F}_3(\boldsymbol{U}) \end{bmatrix}^T, \qquad \boldsymbol{F}_i = \begin{bmatrix} -e_i \times \boldsymbol{H} \\ e_i \times \boldsymbol{E} \end{bmatrix},$$

and

$$\boldsymbol{\alpha} = \begin{bmatrix} \epsilon_r & 0 \\ 0 & \mu_r \end{bmatrix}, \qquad \boldsymbol{J} = \begin{bmatrix} \boldsymbol{J}_E \\ \boldsymbol{J}_H \end{bmatrix}.$$

Consider a partition of the bounded domain $\Omega \subset \mathbb{R}^3$ into a tetrahedral mesh $\overline{\Omega}_T = \bigcup_{i=1}^N \overline{T}_i$. It is assumed that material properties are constant in each cell T_i. Integrating (4) over each tetrahedron T_i and defining the cell averaged values of a given function u as $\bar{u}_i = (1/|T_i|)\int_{T_i} u\, dV$, the semidiscrete finite volume scheme for Maxwell's equations is derived:

$$\boldsymbol{\alpha}_i \frac{\partial \overline{\boldsymbol{U}}_i}{\partial t} + \frac{1}{|T_i|}\int_{\partial T_i} \hat{\boldsymbol{n}} \cdot \boldsymbol{F}\, dS = \boldsymbol{\alpha}_i \frac{\partial \overline{\boldsymbol{U}}_i}{\partial t} + \frac{1}{|T_i|}\sum_{j=1}^{4} |S_{ij}| \hat{\boldsymbol{n}} \cdot \boldsymbol{F}|_{S_{ij}} = \boldsymbol{J}_i, \tag{5}$$

where $\hat{\boldsymbol{n}}$ is the outward unit normal of the tetrahedron boundary ∂T_i consisting of four triangular surfaces S_{ij}, $j = 1, \ldots, 4$. Fluxes in (6) are computed using physical properties on elements T_i and T_j. Physical properties are the same inside homogenous media and different on boundaries between dielectrics. To approximate

the flux on each triangular surface S_{ij}, an upwind scheme based on the Steger–Warming flux vector splitting [30] is used. The splitting is based on the method of characteristics and separates the flux on a face into outgoing and incoming parts according to the sign of the eigenvalues of a 6×6 flux matrix [7]. An application of the flux splitting on each face S_{ij} of a tetrahedron T_i gives the upwind finite volume scheme

$$\hat{\boldsymbol{n}} \cdot \boldsymbol{F}|_{S_{ij}} = \begin{bmatrix} -\hat{\boldsymbol{n}}_{ij} \times [\hat{\boldsymbol{n}}_{ij} \times (\boldsymbol{E}_{ij} - \boldsymbol{E}_{ji}) + (Z_i \boldsymbol{H}_{ij} + Z_j \boldsymbol{H}_{ji})]/(Z_i + Z_j) \\ \hat{\boldsymbol{n}}_{ij} \times [-\hat{\boldsymbol{n}}_{ij} \times (\boldsymbol{H}_{ij} - \boldsymbol{H}_{ji}) + (Y_i \boldsymbol{E}_{ij} + Y_j \boldsymbol{E}_{ji})]/(Y_i + Y_j) \end{bmatrix}, \quad (6)$$

where $Z_i = \sqrt{\mu_i/\epsilon_i}$ denotes the intrinsic impedance, $Y_i = Z_i^{-1}$, and $\hat{\boldsymbol{n}}_{ij}$ denotes the outward unit normal of S_{ij}. The surface averaged electromagnetic fields consisting of outgoing $(\boldsymbol{E}_{ij}, \boldsymbol{H}_{ij})$ and incoming $(\boldsymbol{E}_{ji}, \boldsymbol{H}_{ji})$ plane wave contributions are approximated with the desired accuracy from cell averaged values on T_i and its neighbors. Third order approximations of the field components can be obtained with the four-point Gaussian quadrature rule [18; 33]

$$\boldsymbol{U}_{ij} = \sum_{k=1}^{4} g_k \boldsymbol{U}(\boldsymbol{x}_k^{(j)}), \quad (7)$$

where g_k and $\boldsymbol{x}_k^{(j)}$ are the Gaussian quadrature weights and points, respectively. At each Gaussian quadrature point $\boldsymbol{x}_k^{(j)}$, a third order WENO reconstruction is implemented to approximate the components of $\boldsymbol{U}(\boldsymbol{x}_k^{(j)})$ using the fields averages.

3. Third order WENO reconstruction on tetrahedra

In this work we employ the type II third order WENO scheme developed by Zhang and Shu [33]. Its key idea is to construct a nonlinear combination of second order reconstructions on small stencils $\{S_l\}_{l=1}^{s}$ that gives a third order accurate approximation of a smooth solution on the big stencil $S = \bigcup_{l=1}^{s} S_l$ for each quadrature point $\boldsymbol{x}_k^{(j)}$. Therefore, the main advantage over the type I WENO scheme is that much more compact stencils are used to achieve third order accurate nonoscillatory numerical solutions.

The big stencil $S = \{V_m\}_{m=0}^{r}$ is formed by the cell $V_0 = T_i$ and two layers of its neighbors, and consists of $r \leq 17$ elements. A third order approximation of u at each quadrature point $\boldsymbol{x}_k^{(j)}$ is obtained from a quadratic polynomial $p_2(\boldsymbol{x})$ for which

$$\bar{u}_0 = \frac{1}{|V_0|} \int_{V_0} p_2(\boldsymbol{x})\, dV. \quad (8)$$

In local variables

$$\boldsymbol{\xi} = (\xi_1, \xi_2, \xi_3) = \boldsymbol{\xi}(\boldsymbol{x}) = \frac{\boldsymbol{x} - \boldsymbol{x}_0}{h}, \quad h = |V_0|^{1/3}, \quad (9)$$

where $\boldsymbol{x}_0$ is the barycenter of V_0, the quadratic polynomial $p_2(\boldsymbol{x})$ can be written as

$$p_2(\boldsymbol{x}) = \sum_{0 \le i_1+i_2+i_3 \le 2} a_{i_1 i_2 i_3} \xi_1^{i_1} \xi_2^{i_2} \xi_3^{i_3}. \tag{10}$$

Coefficients $a_{i_1 i_2 i_3}$ are computed by matching the cell averages of $p_2(\boldsymbol{x})$ on every element of $S \setminus \{V_0\}$ to the cell averages of u in a least square sense [4]. To avoid computation of integrals $[\xi_1^{i_1} \xi_2^{i_2} \xi_3^{i_3}]_m$ over each element V_m, we use the approach from [22]. At the k-th quadrature point on the j-th face $\boldsymbol{x}_k^{(j)}$, the third order reconstruction polynomial is given by

$$p_2(\boldsymbol{x}_k^{(j)}) = \sum_{m=0}^{r} c_m \bar{u}_m. \tag{11}$$

The coefficients c_m, $m = 1, \ldots, r$, depend on the geometry only and are precomputed for each quadrature point $\boldsymbol{x}_k^{(j)}$ at initialization.

Each small stencil consists of four elements from the big stencil, and includes the target element V_0. Typically there are up to $s = 16$ candidates for small stencils $\bigcup_{l=1}^{s} S_l = S$ [33]. For each small stencil $S_l = V_0 \cup \{V_m^{(l)}\}_{m=1}^{3}$, a linear polynomial $p_1^{(l)}(\boldsymbol{x}) = a_0^{(l)} + \sum_{i=1}^{3} a_i^{(l)} \xi_i$ is constructed using a similar procedure as for $p_2(\boldsymbol{x}_k^{(j)})$. Just as with the big stencil, the coefficients $c_m^{(l)}$ in

$$p_1^{(l)}(\boldsymbol{x}_k^{(j)}) = \sum_{m=0}^{3} c_m^{(l)} \bar{u}_m^{(l)} \tag{12}$$

depend on the local geometry only and are precomputed at initialization.

A third order type II WENO reconstruction is built as a nonlinear combination of linear polynomials $p_1^{(l)}$. The nonlinear weights of the WENO scheme are defined using the weights of the third order linear reconstruction. For each quadrature point $\boldsymbol{x}_k^{(j)}$ of the face S_j, the linear weights $\{\gamma_l\}_{l=1}^{s}$ are such that the linear combination of polynomials $p_1^{(l)} \boldsymbol{x}_k^{(j)}$ is closest to $p_2 \boldsymbol{x}_k^{(j)}$. The weights for each Gaussian point are found from the system of linear equations constructed from two parts. The first part is formed by taking $u = 1, \xi_1^2, \xi_2^2, \xi_3^2, \xi_1\xi_2, \xi_1\xi_3, \xi_2\xi_3$ in

$$u(\boldsymbol{x}_k^{(j)}) = \sum_{l=1}^{s} \gamma_l p_1^{(l)}(\boldsymbol{x}_k^{(j)}). \tag{13}$$

The second part is constructed using the requirement that

$$p_2(\boldsymbol{x}_k^{(j)}) \overset{1}{=} \sum_{l=1}^{s} \gamma_l p_1^{(l)}(\boldsymbol{x}_k^{(j)}) \tag{14}$$

holds for an arbitrary u, where $\overset{1}{=}$ represents the equality in the least square sense. Solution of two systems together gives the optimal linear weights for the type II

third order linear reconstruction of u at the quadrature point $\boldsymbol{x}_k^{(j)}$:

$$u^{\mathrm{Lin}}(\boldsymbol{x}_k^{(j)}) = \sum_{l=1}^{s} \gamma_l p_1^{(l)}(\boldsymbol{x}_k^{(j)}). \tag{15}$$

While the reconstruction based on linear weights works well for smooth solutions and relatively good unstructured meshes, our goal is to adapt it to the case where the solution is not smooth and the mesh quality is arbitrary. We still take a linear combination of the reconstructions using small stencils, but now so-called nonlinear weights $\{\omega_l\}_{l=1}^{s}$ are employed. Those are designed so that $\omega_l \approx \gamma_l$ in cells where the solution is smooth (so third order accuracy is maintained) and $\omega_l \approx 0$ otherwise to suppress oscillations. The classic WENO weights are defined as

$$\omega_l = \frac{\tilde{\omega}_l}{\sum_{m=1}^{s} \tilde{\omega}_m}, \quad \tilde{\omega}_l = \frac{\gamma_l}{(\epsilon + \mathrm{SI}_l)^2}, \tag{16}$$

where ϵ is a small number traditionally chosen to be between 10^{-2} and 10^{-40} to avoid division by zero, and SI_l is the smoothness indicator on the l-th small stencil:

$$\mathrm{SI}_l = \sum_{i=1}^{3} \int_{T_0} |T_0|^{-1/3} \left(\frac{\partial p_1^{(l)}(\boldsymbol{x})}{\partial x_i} \right)^2 dV. \tag{17}$$

As was pointed out in [2; 17], the choice of ϵ has a crucial effect on the accuracy of classic 1D WENO reconstructions. It was shown that $\mathrm{SI}_l \sim h^2$ for smooth solutions and $\mathrm{SI}_l \sim h^4$ near critical points, suggesting $\epsilon \sim h^2$ as an optimal choice to preserve the accuracy near critical points. Assuming that this dependence is even more important for reconstructions on 3D unstructured meshes with high ratios between linear cell sizes, we implemented the choices

$$\epsilon_i = h_i^k, \quad k = 1, 2, 4, \tag{18}$$

in numerical experiments. These choices are based on the accuracy analysis for the 1D WENO3 scheme which will be presented in the next section. As suggested in [33] we also employ the mapped weights technique [17].

Now to form the type II WENO reconstruction at the point $\boldsymbol{x}_k^{(j)}$, we replace the linear weights γ_l in (15) by the nonlinear ω_l defined in (16)

$$u^{\mathrm{WENO}}(\boldsymbol{x}_k^{(j)}) = \sum_{l=1}^{s} \omega_l p_1^{(l)}(\boldsymbol{x}_k^{(j)}). \tag{19}$$

Since the type II WENO scheme uses smaller stencils than type I WENO, linear weights are completely dependent on the geometry. In 3D problems with complex geometry, the mesh quality is hard to control. The least square solution for linear weights always gives some negative weights. For mildly negative weights, the

splitting technique from [27] is implemented. But on unstructured meshes there is always a small percentage of large negative linear weights which compromise the stability of the computation. To overcome this Liu and Zhang in [21] proposed to replace approximations for which

$$\max_l(|\gamma_l|) > \zeta, \quad 1 \le \zeta \le 10, \tag{20}$$

by a more expensive type I WENO reconstruction. To have the same compact stencil in all reconstructions, we replace a type II WENO reconstruction at quadrature points where (20) holds with a third order polynomial reconstruction (11). In numerical experiments we did not encounter any problem with such substitution even for discontinuous solutions. This can be explained by the fact that very negative linear weights appear only for some quadrature points of a given face. As a result the surface integral (7) is a combination of both WENO and polynomial reconstructions. Therefore, the WENO scheme partially compensates for the oscillatory effect of the polynomial scheme. While using ζ values of up to 10 gives good results on 2D triangular meshes [21], we used the upper limit of $\zeta = 1$ on 3D tetrahedral meshes for stability.

The CPU time for computations using a WENO scheme is significantly larger than that for third order polynomial schemes. Therefore, from a practical point of view, WENO schemes should only be used when their nonoscillatory properties benefit the solution. One way to reduce computational cost is to switch between polynomial and WENO reconstructions depending on the values of smoothness indicators. A naive criterion, such as

$$\max_l \mathrm{SI}_l > \frac{\epsilon}{2}, \tag{21}$$

for WENO reconstruction can significantly reduce the computational time without compromising either the smooth or discontinuous numerical solutions. This is referred to as accelerated WENO (WENOA) in the numerical experiments.

4. Accuracy of third order WENO scheme on nonuniform grid in 1D

Since the numerical solution of 3D Maxwell's equations using a WENO scheme with a fixed small value of ϵ in (16) has unpredictable accuracy, we turned to a 1D theory for selecting a proper value of ϵ. It was shown by Aràndiga et al. in [2] that the accuracy of WENO schemes in 1D can be controlled by defining ϵ based on the mesh size h. The focus of this section is on an analysis of a third order WENO scheme for 1D nonuniform meshes. We use it as a guideline to choose ϵ in 3D simulations.

Consider a nonuniform 1D mesh $a = x_{1/2} < \cdots < x_{i-1/2} < x_{i+1/2} < x_{i+3/2} < \cdots < x_{N+1/2} = b$ with sizes $h_i = x_{i+1/2} - x_{i-1/2}$ on an interval $I_i = [x_{i-1/2}, x_{i+1/2}]$.

The linear polynomials $p_{1,i}^{(l)}(x)$ defined on small stencils $S_i^{(l)} = \{I_{i+l-2}, I_{i+l-1}\}$, $l = 1, 2$, can be obtained as

$$p_{1,i}^{(l)}(x) = \bar{u}_i + \frac{2h_i}{h_{i+l-2} + h_{i+l-1}}[\bar{u}_{i+l-1} - \bar{u}_{i+l-2}]\xi, \quad l = 1, 2. \tag{22}$$

The classic WENO3 weights in 1D are defined by [20; 19]

$$\omega_{l,i} = \frac{\tilde{\omega}_{l,i}}{\tilde{\omega}_{1,i} + \tilde{\omega}_{2,i}} \quad \text{with } \tilde{\omega}_{l,i} = \frac{\gamma_l}{(\epsilon + \mathrm{SI}_{l,i})^p}, \ l = 1, 2, \tag{23}$$

where the linear weights are given by $\gamma_1 = \frac{1}{3}$ and $\gamma_2 = \frac{2}{3}$, and the smoothness indicators $\mathrm{SI}_{l,i}$, $l = 1, 2$, can obtained as

$$\mathrm{SI}_{l,i} = h_i \int_{I_i} (p_{1,i}^{(l)}(x))_x^2 \, dx = \frac{4h_i^2}{(h_{i+l-2} + h_{i+l-1})^2}[\bar{u}_{i+l-1} - \bar{u}_{i+l-2}]^2, \quad l = 1, 2. \tag{24}$$

If $u(x)$ is a smooth function on the big stencil $S_i = \bigcup_{l=1}^{2} S_i^{(l)}$, then the finite volume WENO3 reconstruction with weights given by (23) has the accuracy property [19]

$$u_{i+1/2}^{\mathrm{WENO}} = u(x_{i+1/2}) + O(h^{2+k}), \tag{25}$$

provided that

$$\omega_{l,i} = \gamma_l + O(h^k), \quad k \in \{0, 1\}, \ l = 1, 2. \tag{26}$$

Theorem 1. *Let $u(x) \in C^3$ on the big stencil S_i. Then the smoothness indicators (24) have the following properties.*

(1) *If $u'(x) \neq 0$ for all $x \in S_i$, then*

$$\mathrm{SI}_{l,i} = \alpha_i(x_i)h_i^2 + O(h_i^3), \quad l \in \{1, 2\}, \tag{27}$$

$$\mathrm{SI}_{2,i} - \mathrm{SI}_{1,i} = \beta_i(x_i)h_i^3 + O(h_i^4) \tag{28}$$

for some locally Lipschitz continuous $\alpha_i(x)$ and $\beta_i(x)$.

(2) *If $u(x)$ has a point $x^* \in S_i \setminus \{x_i\}$ such that $u'(x^*) = 0$, then*

$$\mathrm{SI}_{l,i} = \alpha_{l,i}(x_i)h_i^4 + O(h_i^5), \quad l \in \{1, 2\}, \tag{29}$$

$$\mathrm{SI}_{2,i} - \mathrm{SI}_{1,i} = \beta_i(x_i)h_i^4 + O(h_i^5) \tag{30}$$

for some locally Lipschitz continuous $\alpha_{l,i}(x)$ and $\beta_i(x)$.

Proof. Using the Taylor series of the primitive function $U(x) = \int_{-\infty}^{x} u(\xi)\,d\xi$ about x_i, we get

$$\begin{aligned}\mathrm{SI}_{1,i} &= \frac{4h_i^2}{(h_{i-1}+h_i)^2}[\bar{u}_i - \bar{u}_{i-1}]^2 \\ &= \frac{4h_i^2}{(h_{i-1}+h_i)^2}\left(\frac{U(x_i+\frac{1}{2}h_i)-U(x_i-\frac{1}{2}h_i)}{h_i} - \frac{U(x_i-\frac{1}{2}h_i)-U(x_i-\frac{1}{2}h_i-h_{i-1})}{h_{i-1}}\right)^2 \\ &= \left(u'(x_i)h_i - \tfrac{1}{3}u''(x_i)(\tfrac{1}{2}h_i + h_{i-1})h_i + O(h_i^3)\right)^2.\end{aligned}$$

Similarly one can get

$$\mathrm{SI}_{2,i} = \left(u'(x_i)h_i + \tfrac{1}{3}u''(x_i)(\tfrac{1}{2}h_i + h_{i+1})h_i + O(h_i^3)\right)^2.$$

Let $\kappa_l = h_i/h_{i-2l-3}$; then

$$\mathrm{SI}_{l,i} = \left(u'(x_i)h_i + (\tfrac{2}{3}l - 1)(\tfrac{1}{2} + \kappa_l)u''(x_i)h_i^2 + O(h_i^3)\right)^2. \tag{31}$$

Therefore, we deduce (27) and (28) with

$$\alpha_i(x_i) = [u'(x_i)]^2, \qquad \beta_i(x_i) = \frac{1+\kappa_1+\kappa_2}{3}u'(x_i)u''(x_i).$$

Now consider the case when $u'(x^*) = 0$ for some $x^* \in S_i \setminus \{x_i\}$. Let $x_i - x^* = \kappa h_i$ with $0 < |\kappa| < \frac{3}{2}$. Then using the Taylor series of $u'(x)$ about x_i at x^*, we get

$$u'(x_i) = u''(x_i)\kappa h_i + O(h_i^2),$$

which is then substituted into (31) to derive

$$\mathrm{SI}_{l,i} = (\delta_l u''(x_i)h_i^2 + O(h_i^3))^2,$$

where $\delta_l = \kappa + (\frac{2}{3}l - 1)(\frac{1}{2} + \kappa_l)$. Therefore, we obtain the estimates (29) and (30) with $\alpha_{l,i}(x_i) = [\delta_l u''(x_i)]^2$ and $\beta_i(x_i) = (\delta_2^2 - \delta_1^2)[u''(x_i)]^2$. □

Theorem 2. *Let $u(x) \in C^3$ on the big stencil S_i, and $\epsilon = Mh^m$ in (23), for some $M > 0$ and $m \geq 0$. Then the following hold.*

(1) *If $u'(x) \neq 0$ for all $x \in S_i$, then*

$$u_{i+1/2}^{\mathrm{WENO}} - u(x_{i+1/2}) = O(h^3). \tag{32}$$

(2) *If there is a point $x^* \in S_i \setminus \{x_i\}$ such that $u'(x^*) = 0$, then*

$$u_{i+1/2}^{\mathrm{WENO}} - u(x_{i+1/2}) = \begin{cases} O(h^3), & m \leq 3, \\ O(h^2), & m \geq 4. \end{cases} \tag{33}$$

Proof. As in [2] we start by writing

$$\frac{1}{(\epsilon + \mathrm{SI}_{1,i})^p} = \frac{1}{(\epsilon + \mathrm{SI}_{2,i})^p}\left(1 + \frac{\mathrm{SI}_{2,i} - \mathrm{SI}_{1,i}}{\epsilon + \mathrm{SI}_{1,i}}\right)^p. \tag{34}$$

(1) Consider the case when $u'(x) \neq 0$ for all $x \in S_i$. Then using (27) and (28),

$$\frac{\mathrm{SI}_{2,i} - \mathrm{SI}_{1,i}}{\epsilon + \mathrm{SI}_{1,i}} = \frac{p\beta_i(x_i)}{\eta_1 M + \eta_2 \alpha_i(x_i)} h^r + O(h^{r+1}), \tag{35}$$

where

$$r = \max(1, 3-m) \geq 1, \qquad \eta_1 = \begin{cases} 1, & m \leq 2, \\ 0, & m > 2, \end{cases} \qquad \eta_2 = \begin{cases} 0, & m < 2, \\ 1, & m \geq 2. \end{cases}$$

Using (35) in (34) and substituting into (23), we get

$$\tilde{\omega}_{1,i} + \tilde{\omega}_{2,i} = \frac{1}{(\epsilon + \mathrm{SI}_{2,i})^p} (1 + \gamma_1 \nu_{1,i}(x_i) h^r + O(h^{r+1})),$$

where $\nu_{1,i} = p\beta_i(x_i)/(\eta_1 M + \eta_2 \alpha_i(x_i))$ is a locally Lipschitz continuous function. Then

$$\omega_{2,i} = \frac{\gamma_2}{1 + \gamma_1 \nu_{1,i}(x_i) h^r + O(h^{r+1})} = \gamma_2 + O(h^r).$$

Following the same steps, one can derive the same estimate for $\omega_{1,i}$. From (26) and (25) we deduce that (32) holds on S_i regardless of the value of ϵ.

(2) Now assume that at some point $x^* \in S_i \setminus \{x_i\}$, we have $u'(x^*) = 0$. Then

$$\frac{\mathrm{SI}_{2,i} - \mathrm{SI}_{1,i}}{\epsilon + \mathrm{SI}_{1,i}} = \frac{\beta_i(x_i) h^r}{\eta_1 M + \eta_2 \alpha_{1,i}(x_i)} + O(h^{r+1}), \tag{36}$$

where

$$r = \max(0, 4-m) \geq 0, \qquad \eta_1 = \begin{cases} 1, & m \leq 4, \\ 0, & m > 4, \end{cases} \qquad \eta_2 = \begin{cases} 0, & m < 4, \\ 1, & m \geq 4. \end{cases}$$

Following the same steps as before for $m \leq 3$, we get the third order estimate in (33). For $m \geq 4$ using (36) in (34) we get that

$$\frac{1}{(\epsilon + \mathrm{SI}_{1,i})^p} = \frac{1}{(\epsilon + \mathrm{SI}_{2,i})^p} [1 + \nu_{1,i}(x_i) + O(h)],$$

where $\nu_{1,i}(x_i) = (1 + \beta_i(x_i)/(\eta_1 M + \alpha_{1,i}(x_i)))^p - 1$ is a locally Lipschitz continuous function. Therefore,

$$\omega_{2,i} = \frac{\gamma_2}{(1 + \gamma_1 \nu_{1,i}(x_i) + O(h))} = \frac{\gamma_2}{(1 + \gamma_1 \nu_{1,i}(x_i))} + O(h) + \gamma_2 - \gamma_2 = \gamma_2 + O(1).$$

The same result can be obtained for $\omega_{1,i}$. As follows from (25)–(26) for $m \geq 4$, WENO3 gives only second order reconstruction near the critical point x^*. □

Theorem 3. *Let $u(x)$ be a piecewise smooth function with a jump discontinuity $[u^*] = [u(x^*)]$ in $S_i \setminus S_i^{(l)}$, $l \in \{1, 2\}$, at the point x^*. If $\epsilon = Mh^m$, where $m \geq 1$, in (23), then the WENO3 reconstruction with weights defined by (16) gives*

$$u_{i+1/2}^{\mathrm{WENO}} = u(x_{i+1/2}) + O(h^2). \tag{37}$$

Proof. Assume that $x^* \in S_i \setminus S_i^{(1)}$; then we have

$$u_{i+1/2}^{(1)} = u(x_{i+1/2}) + O(h^2), \qquad u_{i+1/2}^{(2)} = u(x_{i+1/2}) + O([u^*]). \tag{38}$$

Since $\mathrm{SI}_{1,i} = O(h^r)$, $r \in \{2, 4\}$, and $\mathrm{SI}_{2,i} = O([u^*]^2)$ for $\epsilon = O(h^m)$, we get

$$\omega_{1,i} = O(h^{2\min(m,r)}[u^*]^{-4}), \qquad \omega_{2,i} = O(1). \tag{39}$$

Therefore,

$$u_{i+1/2}^{\mathrm{WENO}} = \omega_{1,i} u_{i+1/2}^{(1)} + \omega_{2,i} u_{i+1/2}^{(2)} = u(x_{i+1/2}) + O(h^{2\min(m,r)}[u^*]^{-3}) + O(h^2), \tag{40}$$

which, for $m \geq 1$, gives (37). □

Numerical experiments support the validity of the above theory in 1D. Since it would be much more difficult to analyze the general 3D case with unstructured meshes, we use the analysis above to choose ϵ in (16) for our 3D experiments.

5. Numerical examples

In this section a set of 3D electromagnetic (EM) test problems that include plane wave propagation in a parallel plate waveguide, the scattering of a plane wave from a perfectly conducting (PEC) sphere, and plane wave reflection/transmission through a dielectric prism are discussed. Numerical experiments were carried out on an Intel i7-4790k 4.4 GHz quad core CPU with 32 GB of RAM. C++ OpenMP is used to utilize multicore architecture. For the temporal discretization we employ the third order strong stability-preserving (SSP) Runge–Kutta scheme [28].

Example 1: parallel plate waveguide. Consider the problem of a plane wave propagation in a parallel plate wave guide. In this example the computational domain is represented by a cube with linear size $l = 2$ m. We impose PEC boundary conditions on cube faces parallel to the x-y plane, and PMC boundary condition on two faces parallel to the z-x plane. A plane wave excited at $x = -1$ and propagating in x direction is given by the boundary conditions

$$E_z^{\mathrm{in}} = f(t), \quad H_y^{\mathrm{in}} = -f(t)\epsilon_0^{1/2}\mu_0^{-1/2}, \quad E_x^{\mathrm{in}} = E_y^{\mathrm{in}} = H_x^{\mathrm{in}} = H_z^{\mathrm{in}} = 0. \tag{41}$$

The geometry of the problem is shown in Figure 1.

First consider an incoming plane wave (41) given by the Gaussian pulse

$$f(t) = e^{-b^{-2}(t-t_0)^2}, \tag{42}$$

where $b = 1.2 \times 10^{-9}$ s and $t_0 = 0.5lc_0^{-1}$. Experiments are performed on meshes with relatively uniform linear size of tetrahedrons equal to 0.2, 0.1, and 0.05. To validate WENO schemes with $\epsilon = h, h^2, h^4$ in (16) (WENO-h, h^2, h^4) the discrete

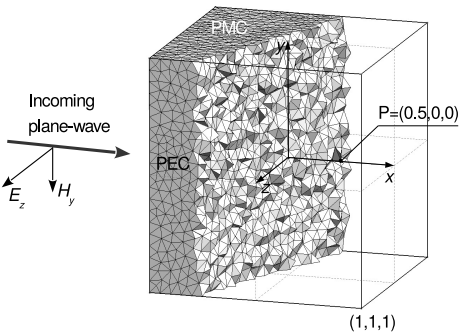

Figure 1. Propagation in a parallel plate waveguide: geometry of the problem.

# of cells	L^2 error	order	L^2 error	order	L^2 error	order
	MUSCL		Polynomial			
8040	$2.747358 \cdot 10^{-2}$		$1.580182 \cdot 10^{-2}$			
64076	$1.263663 \cdot 10^{-2}$	1.12	$2.045965 \cdot 10^{-3}$	2.95		
554668	$6.040267 \cdot 10^{-3}$	1.06	$2.235041 \cdot 10^{-4}$	3.19		
4028196	$3.140725 \cdot 10^{-3}$	0.94				
	WENO-h		WENO-h^2		WENO-h^4	
8040	$1.338234 \cdot 10^{-2}$		$1.409145 \cdot 10^{-2}$		$1.959543 \cdot 10^{-2}$	
64076	$1.942162 \cdot 10^{-3}$	2.78	$2.106160 \cdot 10^{-3}$	2.74	$5.156885 \cdot 10^{-3}$	1.93
554668	$2.133779 \cdot 10^{-4}$	3.19	$2.554968 \cdot 10^{-4}$	3.04	$1.268922 \cdot 10^{-3}$	2.02

Table 1. Propagation in a parallel plate waveguide: L^2 errors at $T = lc_0^{-1} (l = 2\,\mathrm{m})$ for MUSCL, third order polynomial, and WENO-h, h^2, h^4 schemes.

L^2 errors at time $T = lc_0^{-1}$ are computed by

$$l_2(\boldsymbol{U}(T)) = \frac{\left[\sum_{i=1}^{N} |T_i| \sum_{j=1}^{3} \frac{1}{2}(\epsilon_r \epsilon_0 (\bar{E}_i^j)^2 + \mu_r \mu_0 (\bar{H}_i^j)^2)\right]^{1/2}}{\left[\epsilon_0 \sum_{i=1}^{N} |T_i|\right]^{1/2}}. \tag{43}$$

In Table 1 discrete L^2 errors for WENO-h, h^2, h^4 schemes are compared to the ones by MUSCL [7] and third order polynomial schemes. Comparison of time-domain solutions at the observation point $P = (0.5, 0, 0)$ (see Figure 1) is shown in Figure 2. The best resolution of peaks is obtained with WENO-h, while WENO-h^4 significantly distorts the solution near critical points. These results suggest that the 1D theory on the choice of ϵ is applicable to 3D simulations.

Table 2 shows storage requirements as well as the CPU times for MUSCL, WENO, accelerated WENO (WENOA), and polynomial schemes. The speedup achieved by WENOA scheme compared to WENO is due to the application of

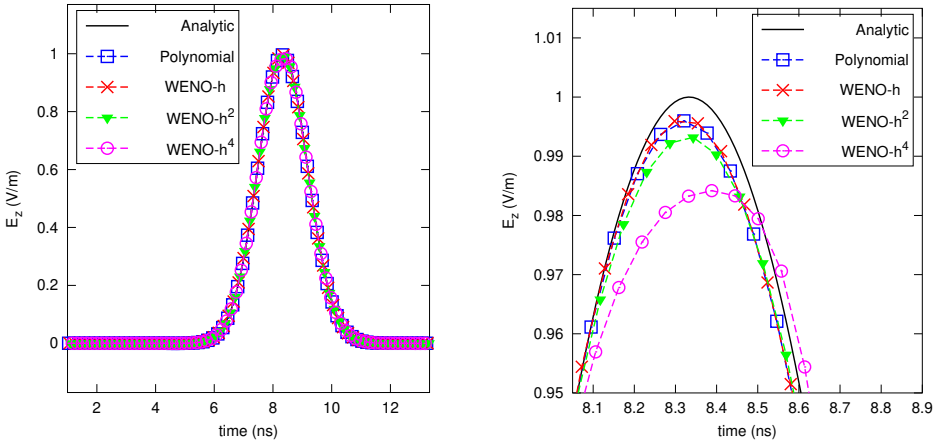

Figure 2. Propagation in a parallel plate waveguide: time-domain solution for the propagation of Gaussian pulse at the observation point (0.5, 0, 0).

# of cells	Storage (GB) MUSCL	Polyn.	WENO	CPU$_T$ (s), $T = lc_0^{-1}$ MUSCL	Polyn.	WENO-h^2	WENOA-h^2
64076	0.04	0.2	1.2	118	197	6601	851
554668	0.3	1.5	11.8	2193	3490	136194	16128
4028196	2.2			31580			

Table 2. Propagation in a parallel plate waveguide: storage and CPU time for MUSCL, third order polynomial, and WENO schemes.

the criterion $\max_l \mathrm{SI}_l > \epsilon/2$ for WENO reconstructions. In this case less than 5% of all flux computations use the expensive WENO approximation. At the same time computation of SI_l itself is computationally expensive, which degrades the performance of WENOA compared to the polynomial scheme. Therefore, a more efficient criterion could further improve the performance of WENOA schemes.

Next consider a discontinuous signal given by

$$f(t) = H(t - t_s)H(t_e - t),$$

where $H(t)$ is the Heaviside step function and $t_s = \frac{1}{8}lc_0^{-1}$ and $t_e = \frac{7}{8}lc_0^{-1}$. Figure 3 shows time-domain solutions of the E_z field at the observation point $P = (0.5, 0, 0)$ using polynomial and WENO-h, h^2, h^4 schemes. The results illustrate that the 1D analysis of the WENO3 scheme for discontinuous solutions regarding the choice of ϵ is also valid for 3D numerical simulations.

Example 2: scattering from a PEC sphere. Consider the classical scattering problem of a plane wave at a PEC sphere for which the analytic series solution is known [14; 3]. The computational domain is represented by a sphere of radius 3 m with

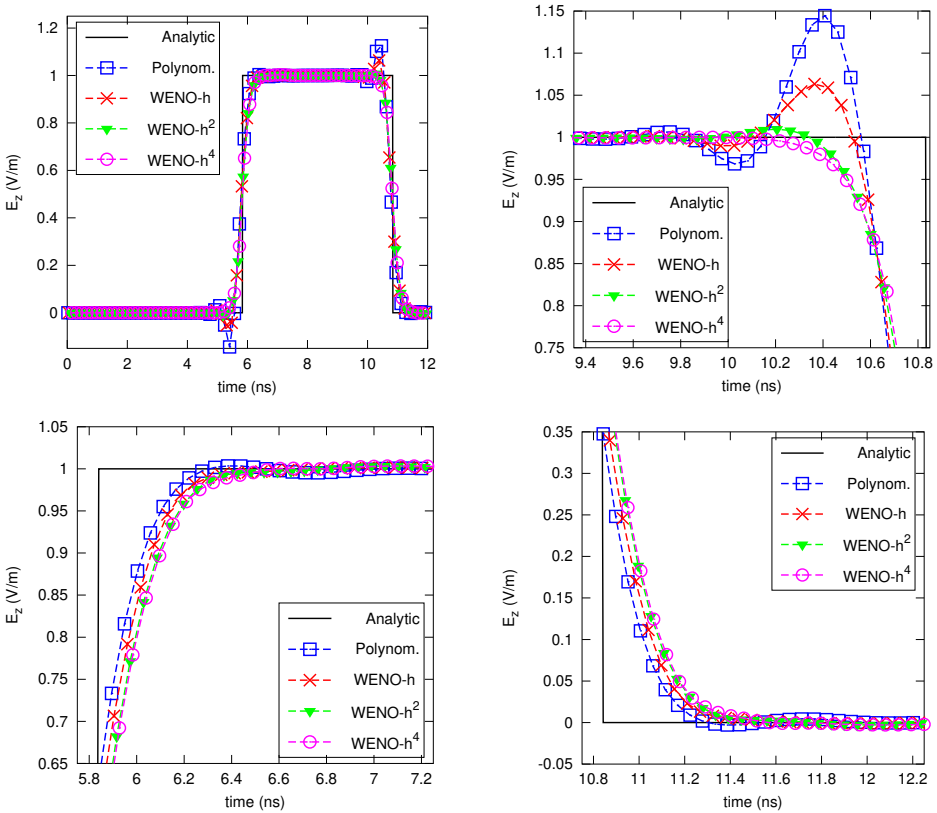

Figure 3. Propagation in a parallel plate waveguide: time-domain solution in time for the propagation of a discontinuous pulse at the observation point (0.5, 0, 0).

a sphere (PEC) of radius 0.5 m cut out at the origin (see Figure 4). The mesh consists of smaller tetrahedrons with average edge length 0.0625 in the region near a PEC surface and larger tetrahedrons with linear size 0.125 at the outer free space boundary. The generated mesh contains 539332 tetrahedra with 2026 of them containing a PEC face. The x component of the electric field of the incident plane wave E_x^I is given by the derivative of the Gaussian pulse

$$E_x^{\text{inc}} = -2\frac{t-t_0}{b^2}Ae^{-(t-t_0)^2/b^2}, \tag{44}$$

where $A = 1.7489 \times 10^{-9}\ \frac{\text{V·s}}{\text{m}}$, $b = 1.5 \times 10^{-9}$ s, and $t_0 = 6 \times 10^{-9}$ s.

The solution of the scattered FVTD formulation using WENO-h_i, h_i^2, h_i^4 schemes as well as the polynomial scheme are compared to the analytic solution at the observation point shown in Figure 4. The results for the E_x field presented in Figure 5 demonstrate that WENO-h_i^4 generates much larger errors than those of WENO-h_i or WENO-h_i^2. This again agrees with the theory for WENO3 in the 1D case.

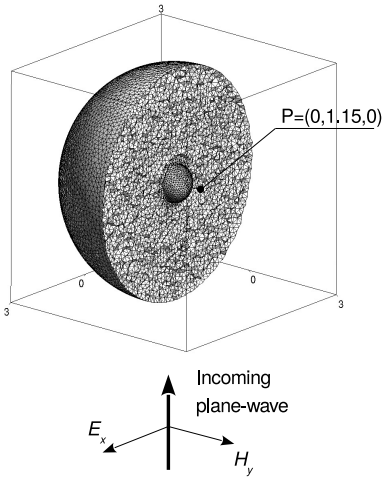

Figure 4. Scattering from PEC sphere: problem geometry and mesh.

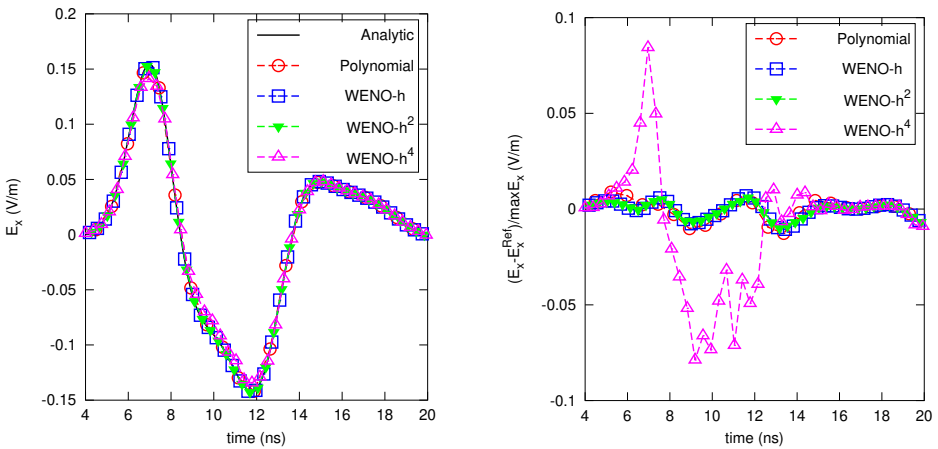

Figure 5. Scattering from PEC sphere: time-domain solution at observation points using third order linear and WENO schemes.

Example 3: glass prism in a waveguide. The last example demonstrates how a WENO scheme handles a problem with inhomogeneous media. This is also the test case where a third order polynomial scheme may not be stable for a reasonable time step. Like in the first example, consider a free space cube domain enclosed between two parallel PEC and two PMC plates. A plane wave signal propagating in the x direction is given by the Gaussian pulse (41)–(42). Inside the cube a glass rhombus prism with dielectric properties $\epsilon_r = 2$ and $\mu_r = 1$ is placed. The dimensions of the prism are shown in Figure 6. Numerical simulation using a third

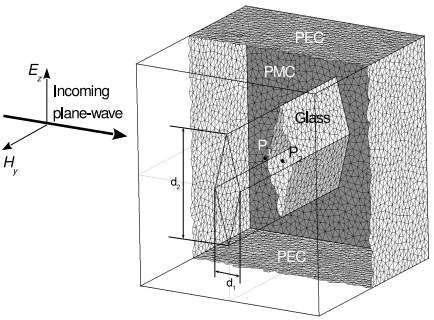

Figure 6. Glass prim in a waveguide: problem geometry and mesh. Observation points shown have coordinates $P_1 = (-0.2, 0, 0)$ and $P_2 = (0, 0, 0)$, and rhombus diagonals are $d_1 = 0.28$ and $d_2 = 1.0$.

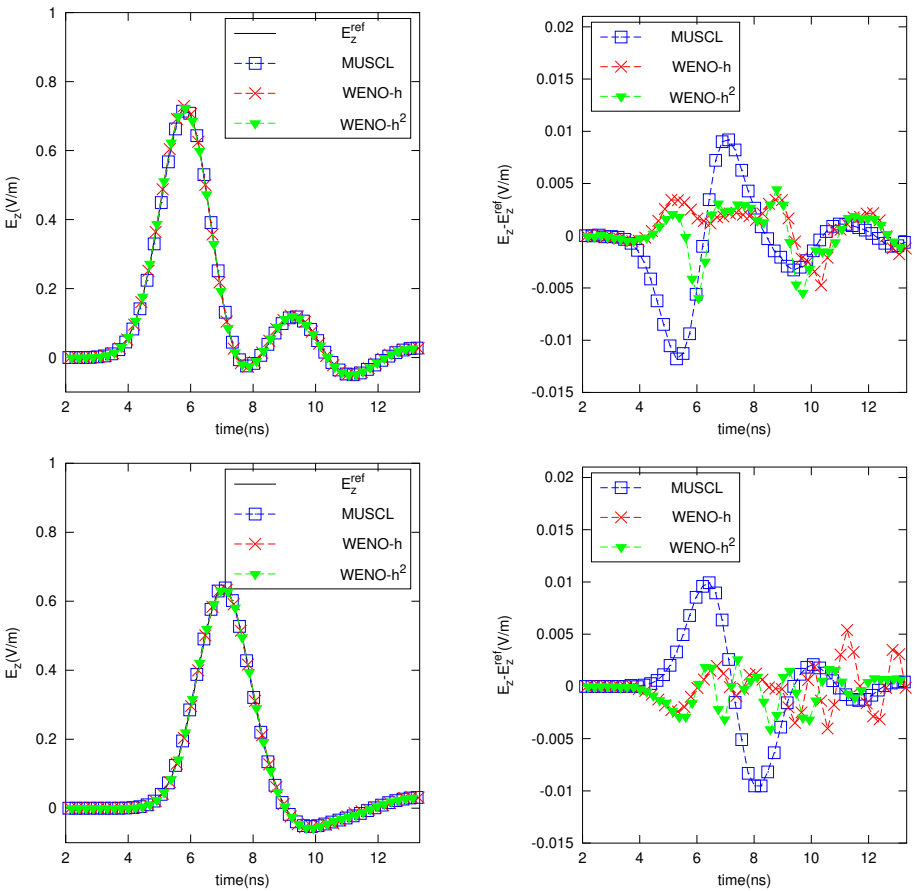

Figure 7. Glass prism in a waveguide: time-domain solution at observation points $P_1 = (-0.2, 0, 0)$ (top row) and $P_2 = (0, 0, 0)$ (bottom row) using MUSCL and WENO-h, h^2 schemes on a mesh with $h = 0.05$ compared to the reference solution by the MUSCL scheme on a mesh with $h = 0.0125$.

order polynomial scheme is unstable for this configuration. Therefore, we only compare numerical results obtained by WENO-h, h^2 schemes on a mesh of average linear cell size 0.05 to the result by the MUSCL scheme [7] on the same mesh. Numerical solution by the MUSCL scheme on a finer mesh with linear cell size 0.0125 is used as a reference solution. Figure 7 shows the time-domain solution for the E_z field as well as a pointwise error with reference solution at two observation points (before and inside the glass prism) shown in Figure 6. We find that while the polynomial scheme diverges for this problem, WENO schemes still converge with better accuracy than the MUSCL scheme. We notice higher level oscillations in the results by the WENO-h scheme compared to WENO-h^2. This suggests WENO-h^2 as a better choice for problems with dielectric contrasts.

6. Summary

In this paper we have successfully implemented a third order type II WENO scheme developed in [33] to solve the linear Maxwell's equations on tetrahedral meshes. An efficient implementation of the scheme is challenging due to its strong dependence on mesh geometry, mesh scale, and high computational cost. Because of the unstructured mesh, the least square solution of the system for finding linear weights almost always contains negative components which create unstable and inaccurate results. To solve this problem we used a hybridization with a third order polynomial scheme at quadrature points with very negative linear weights. Also due to irregular geometries a small number of small stencil matrices are singular. These stencils are removed at the initialization step to avoid polluting the linear scheme. We also implemented specific choices of ϵ dependent on cell sizes in the definition of nonlinear weights which allowed us to control both the accuracy and dissipation in the numerical solution. In our study we used a 1D accuracy analysis as a guideline for the 3D scheme and our numerical experiments confirmed its validity. As in earlier work for uniform meshes in 1D [2], we found that $e = h_i^2$ for each cell is optimal for solutions containing both smooth and singular parts. To reduce computational cost associated with WENO reconstruction, we implemented a criterion that determines which stencils could use cheaper polynomial reconstruction instead. The resulting WENOA-h^2 scheme is more efficient than lower order FV schemes such as MUSCL, and is nonoscillatory and more stable than linear schemes for EM problems with varying material properties and complex geometries.

References

[1] R. Abgrall, *On essentially non-oscillatory schemes on unstructured meshes: analysis and implementation*, J. Comput. Phys. **114** (1994), no. 1, 45–58. MR Zbl

[2] F. Aràndiga, A. Baeza, A. M. Belda, and P. Mulet, *Analysis of WENO schemes for full and global accuracy*, SIAM J. Numer. Anal. **49** (2011), no. 2, 893–915. MR Zbl

[3] C. A. Balanis, *Advanced engineering electromagnetics*, Wiley, 1989.

[4] T. J. Barth and P. O. Frederickson, *Higher order solution of the Euler equations on unstructured grids using quadratic reconstruction*, 28th Aerospace Sciences Meeting, no. 90-0013, AIAA, 1990.

[5] P. Batten, C. Lambert, and D. M. Causon, *Positively conservative high-resolution convection schemes for unstructured elements*, Internat. J. Numer. Methods Engrg. **39** (1996), no. 11, 1821–1838. MR Zbl

[6] D. Baumann, C. Fumeaux, and R. Vahldieck, *Field-based scattering-matrix extraction scheme for the FVTD method exploiting a flux-splitting algorithm*, IEEE T. Microw. Theory **53** (2005), no. 11, 3595–3605.

[7] P. Bonnet, X. Ferrieres, F. Issac, F. Paladian, J. Grando, J. C. Alliot, and J. Fontaine, *Numerical modeling of scattering problems using a time domain finite volume method*, J. Electromagnet. Wave **11** (1997), no. 8, 1165–1189. Zbl

[8] R. Borges, M. Carmona, B. Costa, and W. S. Don, *An improved weighted essentially non-oscillatory scheme for hyperbolic conservation laws*, J. Comput. Phys. **227** (2008), no. 6, 3191–3211. MR Zbl

[9] A. Chatterjee and R.-S. Myong, *Efficient implementation of higher-order finite volume time-domain method for electrically large scatterers*, Prog. Electromagn. Res. B **17** (2009), 233–254.

[10] M. Dumbser and M. Käser, *Arbitrary high order non-oscillatory finite volume schemes on unstructured meshes for linear hyperbolic systems*, J. Comput. Phys. **221** (2007), no. 2, 693–723. MR Zbl

[11] M. Dumbser, M. Käser, V. A. Titarev, and E. F. Toro, *Quadrature-free non-oscillatory finite volume schemes on unstructured meshes for nonlinear hyperbolic systems*, J. Comput. Phys. **226** (2007), no. 1, 204–243. MR Zbl

[12] L. J. Durlofsky, B. Engquist, and S. Osher, *Triangle based adaptive stencils for the solution of hyperbolic conservation laws*, J. Comput. Phys. **98** (1992), no. 1, 64–73. Zbl

[13] D. Firsov, J. LoVetri, I. Jeffrey, V. Okhmatovski, C. Gilmore, and W. Chamma, *High-order FVTD on unstructured grids using an object-oriented computational engine*, ACES J. **22** (2007), no. 1, 71–82.

[14] R. F. Harrington, *Time-harmonic electromagnetic fields*, McGraw-Hill, 1961.

[15] A. Harten and S. R. Chakravarthy, *Multi-dimensional ENO schemes for general geometries*, Tech. Report 187637, NASA, 1991.

[16] A. Harten, B. Engquist, S. Osher, and S. R. Chakravarthy, *Uniformly high-order accurate essentially nonoscillatory schemes, III*, J. Comput. Phys. **71** (1987), no. 2, 231–303. MR Zbl

[17] A. K. Henrick, T. D. Aslam, and J. M. Powers, *Mapped weighted essentially non-oscillatory schemes: achieving optimal order near critical points*, J. Comput. Phys. **207** (2005), no. 2, 542–567. Zbl

[18] P. Hillion, *Numerical integration on a triangle*, Internat. J. Numer. Methods Engrg. **11** (1977), no. 5, 797–815. MR Zbl

[19] G.-S. Jiang and C.-W. Shu, *Efficient implementation of weighted ENO schemes*, J. Comput. Phys. **126** (1996), no. 1, 202–228. MR Zbl

[20] X.-D. Liu, S. Osher, and T. Chan, *Weighted essentially non-oscillatory schemes*, J. Comput. Phys. **115** (1994), no. 1, 200–212. MR Zbl

[21] Y. Liu and Y.-T. Zhang, *A robust reconstruction for unstructured WENO schemes*, J. Sci. Comput. **54** (2013), no. 2–3, 603–621. MR Zbl

[22] C. Ollivier-Gooch and M. Van Altena, *A high-order-accurate unstructured mesh finite-volume scheme for the advection–diffusion equation*, J. Comput. Phys. **181** (2002), no. 2, 729–752. Zbl

[23] S. Piperno, M. Remaki, and L. Fezoui, *A nondiffusive finite volume scheme for the three-dimensional Maxwell's equations on unstructured meshes*, SIAM J. Numer. Anal. **39** (2002), no. 6, 2089–2108. MR Zbl

[24] T. Pringuey and R. S. Cant, *High order schemes on three-dimensional general polyhedral meshes — application to the level set method*, Commun. Comput. Phys. **12** (2012), no. 1, 1–41. MR Zbl

[25] M. Remaki, *A new finite volume scheme for solving Maxwell's system*, COMPEL **19** (2000), no. 3, 913–932. Zbl

[26] V. Shankar, W. F. Hall, and A. H. Mohammadian, *A time-domain differential solver for electromagnetic scattering problems*, Proc. IEEE **77** (1989), no. 5, 709–721.

[27] J. Shi, C. Hu, and C.-W. Shu, *A technique of treating negative weights in WENO schemes*, J. Comput. Phys. **175** (2002), no. 1, 108–127. Zbl

[28] C.-W. Shu and S. Osher, *Efficient implementation of essentially nonoscillatory shock-capturing schemes*, J. Comput. Phys. **77** (1988), no. 2, 439–471. MR Zbl

[29] T. Sonar, *On the construction of essentially non-oscillatory finite volume approximations to hyperbolic conservation laws on general triangulations: polynomial recovery, accuracy and stencil selection*, Comput. Methods Appl. Mech. Engrg. **140** (1997), no. 1–2, 157–181. MR Zbl

[30] J. L. Steger and R. F. Warming, *Flux vector splitting of the inviscid gasdynamic equations with application to finite-difference methods*, J. Comput. Phys. **40** (1981), no. 2, 263–293. MR Zbl

[31] P. Tsoutsanis, V. A. Titarev, and D. Drikakis, *WENO schemes on arbitrary mixed-element unstructured meshes in three space dimensions*, J. Comput. Phys. **230** (2011), no. 4, 1585–1601. MR Zbl

[32] M. Wirianto, W. A. Mulder, and E. C. Slob, *Applying essentially non-oscillatory interpolation to controlled-source electromagnetic modelling*, Geophys. Prospect. **59** (2011), no. 1, 161–175.

[33] Y.-T. Zhang and C.-W. Shu, *Third order WENO scheme on three dimensional tetrahedral meshes*, Commun. Comput. Phys. **5** (2009), no. 2–4, 836–848. MR Zbl

Received March 9, 2017. Revised January 3, 2018.

MARINA KOTOVSHCHIKOVA: m.a.kotovshchikova@gmail.com
Department of Mathematics, University of Manitoba, Winnipeg, Manitoba, Canada

DMITRY K. FIRSOV: d.k.firsov@gmail.com
San Jose, CA, United States

SHIU HONG LUI: luish@cc.umanitoba.ca
Department of Mathematics, University of Manitoba, Winnipeg, Manitoba, Canada

Communications in Applied Mathematics and Computational Science

msp.org/camcos

See inside back cover or msp.org/camcos for submission instructions.

The subscription price for 2018 is US $100/year for the electronic version, and $150/year (+$15, if shipping outside the US) for print and electronic. Subscriptions, requests for back issues from the last three years and changes of subscriber address should be sent to MSP.

Communications in Applied Mathematics and Computational Science (ISSN 2157-5452 electronic, 1559-3940 printed) at Mathematical Sciences Publishers, 798 Evans Hall #3840, c/o University of California, Berkeley, CA 94720-3840, is published continuously online. Periodical rate postage paid at Berkeley, CA 94704, and additional mailing offices.

CAMCoS peer review and production are managed by EditFLOW® from MSP.

PUBLISHED BY

mathematical sciences publishers

nonprofit scientific publishing

http://msp.org/

Communications in Applied Mathematics and Computational Science

vol. 13 no. 1 2018